Auxiliary Material for

Hot upwelling conduit beneath the Atlas Mountains, Morocco

Daoyuan Sun, Meghan S. Miller, Adam F. Holt, Thorsten W. Becker

University of Southern California

Geophysical Research Letters, 2014

Introduction

To generate the seismic waveform synthetics, we applied a 2-D, staggered grid Finite Difference scheme with implementation of accurate point source mechanism [*Li et al.*, 2014]. We used a grid size of 200 m with time step of 0.01 s, which makes the calculation accurate up to 2 Hz. In order to test the trade-off between the velocity perturbation and the depth extent of the low velocity anomaly, we conducted resolution tests to evaluate the different parameters.

The original tomography model [*Bezada et al.*, 2013] predicts travel times well (Fig. S1). However, it is too smooth to predict the sharp travel time jump and secondary arrivals. For a weaker LVA model (δVs = –4%) (Fig. S2), the travel times are shifted to earlier arrivals and the amplitudes are smaller. In contrast, a stronger model (δVs = –8%) has later arrivals and the second arrivals are late and stronger than those in the data. If the length of the LVA is 100 km (Fig. S3), a much stronger shear velocity reduction (~–10%) is needed to explain the travel time change from station PM21 and PM22. However, such a model predicts much later second arrivals than observed in the data. In contrast, if we extend the LVA to 300 km depth (Fig. S4), the reduced shear velocity anomaly matches

the travel time but produces earlier and weaker second arrivals that do not compare to the observations.

The width of the LVA primarily affects the variation of the waveform amplitude near 4º distance. If the anomaly is wider (~110 km, Fig. S5), the region with large amplitude is broad. A narrower anomaly will generate a confined large amplitude zone in the synthetic waveforms that are not observed in the data (Fig. S5). In Fig. S6, we test a high velocity anomaly structure instead of the LVA. Although this model predicts the travel time jump from station PM21 to PM22, it generates very weak secondary late arrivals. By comparing the travel times, amplitudes, and the arrival times between the second and first pulses for all 15 stations along the profile for the deep focus event and the *S-SKS* differential times, we found that a 200 km long and 80 km wide LVA with shear wave velocity perturbation of −6% (Fig. 2) best explained the *S* data. Such an anomaly also explains the observed change in the differential travel time between *S* and *SKS* for teleseismic events. From station PM21 to PM22, while *SKS* travel times stay constant, the sharp *S* travel time delay results *S-SKS* differential travel time increase sharply (Fig. S7).

The differential *P* travel times for teleseismic events display variations of less than ~ 1 sec (Fig. S8). The *P* records of the deep Granada event do not have the second arrivals as in the *S* data (Fig. S9), which suggests the *P* anomaly is much weaker than the *S* anomaly. We tested models with the same geometry as the *S* model and different *P* velocity perturbations. To match the amplitude variation across the profile, a model with *P* velocity drop of 3-4% is preferred (Fig. S9).

In Equation 1, V_0 is the ambient *P* or *S* velocity for AK135 at the depth of 140 km. α is a constant value of 0.15 [*Goes et al.*, 2012], and *Q* is the attenuation quality factor. We adopt the velocity derivatives for the shallow mantle from *Goes et al.* [2000]. We have $\partial V_S/\partial T = -0.3791$ m·s^{-1}·K^{-1} and $\partial V_P/\partial T = -0.5364$ m·s^{-1}·K^{-1}. The melt contribution is added using $\partial V_S/\partial \varphi = -2.04 V_{S0}$ and $\partial \ln V_P/\partial \varphi = -1.23 V_{P0}$ assuming the unrelaxed state [*Kreutzmann et al.*, 2004]. We chose *Qs* from the partly empirical model defined in *Goes et al.* [2012] as

$$Q_S = A_g \left(\frac{C_{OH}^{ref}}{C_{OH}} \right)^s f^{\alpha_g} \exp\left(\frac{\alpha_g \gamma T_m}{T_{ref} + \Delta T} \right)$$

The parameters are A_g = 0.1, α_g = 0.15, γ = 38, s = 0.37. T_m is the melting temperature. In the calculation, we use the dry solidus temperature following *Hirschmann* [2000] with T_m = 1890 K at 4.5 GPa (140 km depth). T_{ref} is the ambient temperature. C_{OH}^{ref} is the reference hydration of the mantle as 1000 H/10^{6}Si. Because the effects of high water content on velocity are similar as those of partial melting [*Karato*, 2004], it is difficult to distinguish them from velocities alone. Thus, we assume a dry mantle with C_{OH} = 50 H/10^{6}Si. *Qs* is also affected by the seismic frequency *f*. Here, the frequency is ~0.25 Hz for *S* waves. For simplicity,

$Q_P = Q_S \frac{3}{4} \left(\frac{V_P}{V_S} \right)^2$ [*Goes et al.*, 2000].

1. fs01.pdf (Figure S1) Comparison between the *S* data and the synthetics for *P* tomography scaled by 1.8.
2. fs02.pdf (Figure S2) Comparison between the *S* data and the synthetics for the Granada earthquake. The model is the same as that in Fig. 3 but with different δVs. From left to right: −6%, −4%, −8%.
3. fs03.pdf (Figure S3) (A) Comparison between the *S* data and the synthetics for the Granada earthquake. The LVA model has the length of 100 km and different δVs. From left to right: −8%, −10%, −12%. (B) travel time and amplitude of the data (black triangles) and the synthetics (lines). The black, red, and blue lines are predictions from the low velocity anomaly with velocity perturbation of −8%, −10%, and −12%, respectively.
4. fs04.pdf (Figure S4) (A) Comparison between the *S* data and the synthetics for the Granada earthquake. The LVA model has the length of 300 km and different δVs. From left to right: −3%, −4%, −5%. (B) travel time and amplitude of the data (black triangles) and the synthetics (lines). The black, red, and blue lines are predictions from the low velocity anomaly with velocity perturbation of −3%, −4%, and −5%, respectively.
5. fs05.pdf (Figure S5) (A) Comparison between the *S* data and the synthetics for the Granada earthquake. The LVA model has the length of 200 km, δVs of −6% and different width. From left to right: 80 km, 50 km, 110 km. (B) travel time and amplitude of the data (black triangles) and the synthetics (lines).
6. fs06.pdf (Figure S6) Prediction from a high velocity model, indicated by blue box in (A). The preferred LVA model is outlined by the orange line. (B) Comparison between the *S* data and the synthetics for the high velocity model.
7. fs07.pdf (Figure S7) Prediction for the teleseimic *S-SKS* differential travel time for an event from the northeastern direction. The red triangles are data. The black line is the prediction from our preferred LVA model in Fig. 3.

8. fs08.pdf (Figure S8) *P* differential travel time between stations PM22 and PM21 against the back-azimuths of the events from station PM21. The star represents the upgoing *P* phase of the deep Granada earthquake. The radius is the incident angle from horizontal at the depth of 120 km assuming the 1-D AK135 reference .

9. fs09.pdf (Figure S9) (A) Comparison between the *P* data and the synthetics for the Granada earthquake. The LVA model has identical shape as that in Fig. 3 but different δVp. From left to right: −3%, −4%, −5%. (B) travel time and amplitude of the data (black triangles) and the synthetics (lines).

10. fs10.pdf (Figure S10) Histograms of estimates of T_{ref}, ΔT, φ, dVp/Vp_0, and dVs/Vs_0 from the Monte Carlo simulations assuming a hydrated mantle with C_{OH} = 300 H/10^6Si and 120 K lower melting temperature than that for the dry solidus.

Reference

Bezada, M. J., E. D. Humphreys, D. R. Toomey, M. Harnafi, J. M. Davila, and J. Gallart (2013), Evidence for slab rollback in westernmost Mediterranean from improved upper mantle imaging, *Earth Planet. Sci. Lett.*, *368*, 51-60.

Goes, S., R. Govers, and P. Vacher (2000), Shallow mantle temperatures under Europe from P and S wave tomography, *J. Geophys. Res.*, *105*(B5), 11153-11169.

Goes, S., J. Armitage, N. Harmon, H. Smith and R. Huismans (2012), Low seismic velocities below mid-oceani ridges: Attenuation versus melt retention, *J. Geophys. Res.*, 117, B124013, doi:10.1029/2012JB009637.

Hirschmann, M. M. (2000), Mantle solidus: Experimental constraints and the effects of peridotite composition, *Geochem. Geophys. Geosyst.*, 1, 1042, doi:10.1029/2000gc000070.

Kreutzmann, A., H. Schmeling, A. Junge, T. Ruedas, G. Marquart, and I. T. Bjarnason

(2004), Temperature and melting of a ridge-centred plume with application to Iceland. Part II: Predictions for electromagnetic and seismic observables, *Geophys. J. Int.*, *159*, 1097–1111. doi: 10.1111/j.1365-1246X.2004.02397.x.

Li, D., D. Helmberger, R. W. Clayton, and D. Sun (2014), Global synthetic seismograms using a 2-D finite-difference method, *Geophys. J. Int.*, *197*(2), 1166-1183. doi: 1110.1093/gji/ggu1050.

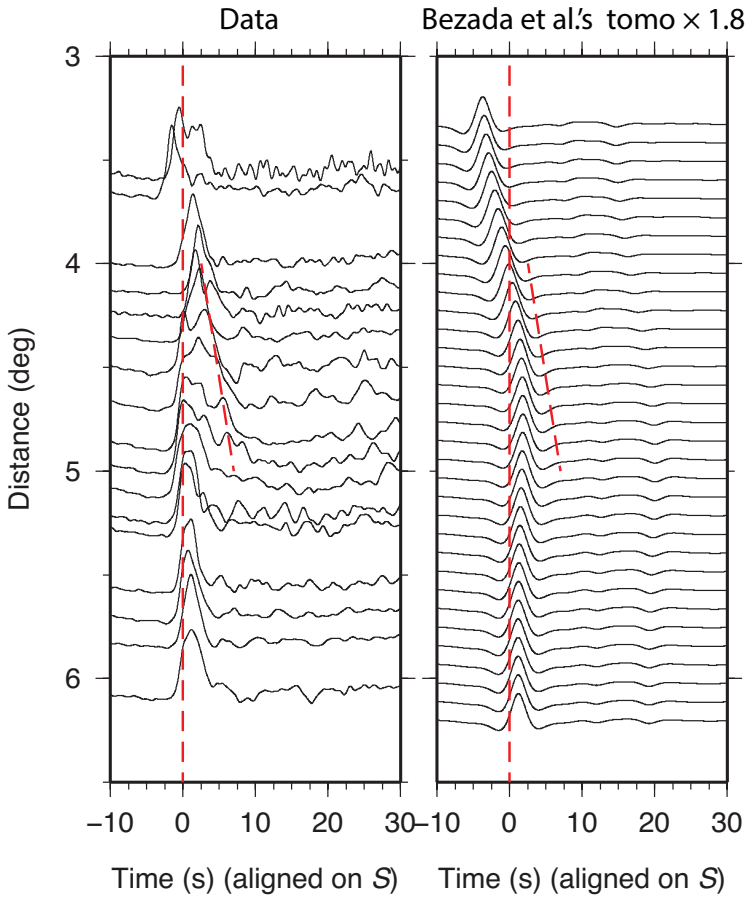
Data
Bezada et al.'s tomo × 1.8
Distance (deg)
3
4
5
6
–10
0
10
20
30
Time (s) (aligned on S)
Time (s) (aligned on S)

Figure S1

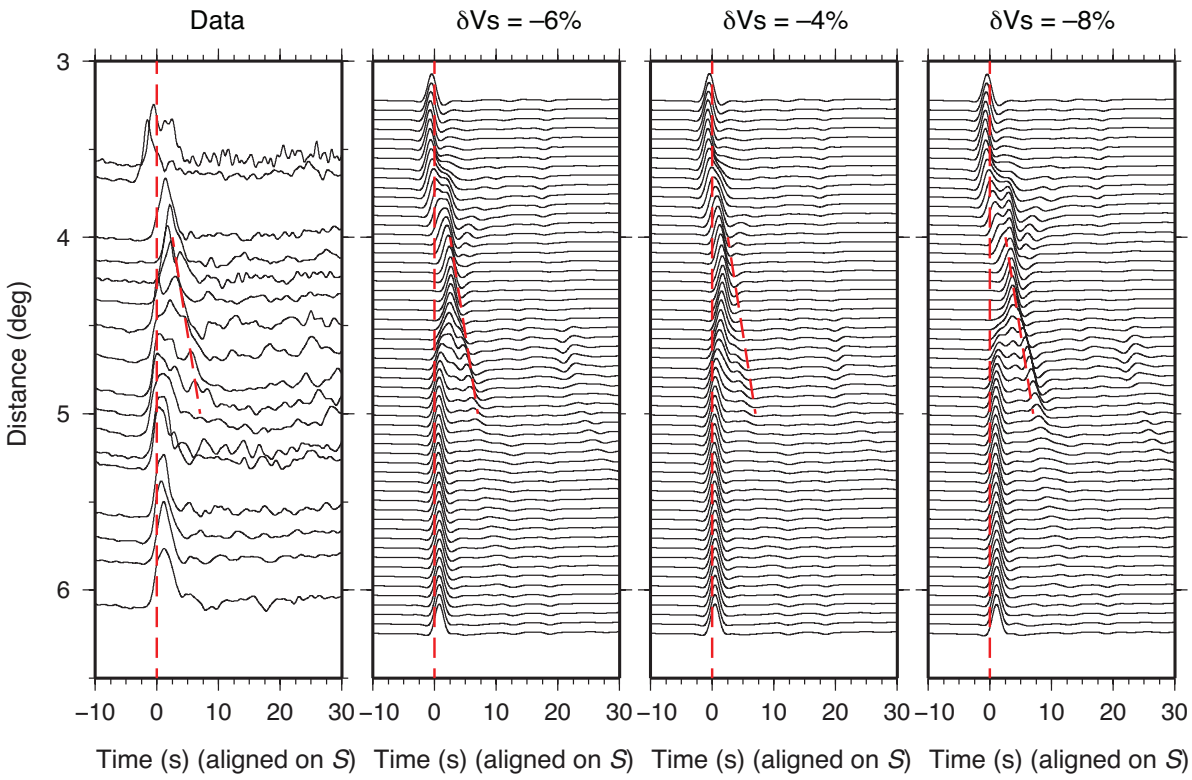
Data
δVs = –6%
δVs = –4%
δVs = –8%
Distance (deg)
3
4
5
6
–10
0
10
20
30
Time (s) (aligned on S)

Figure S2

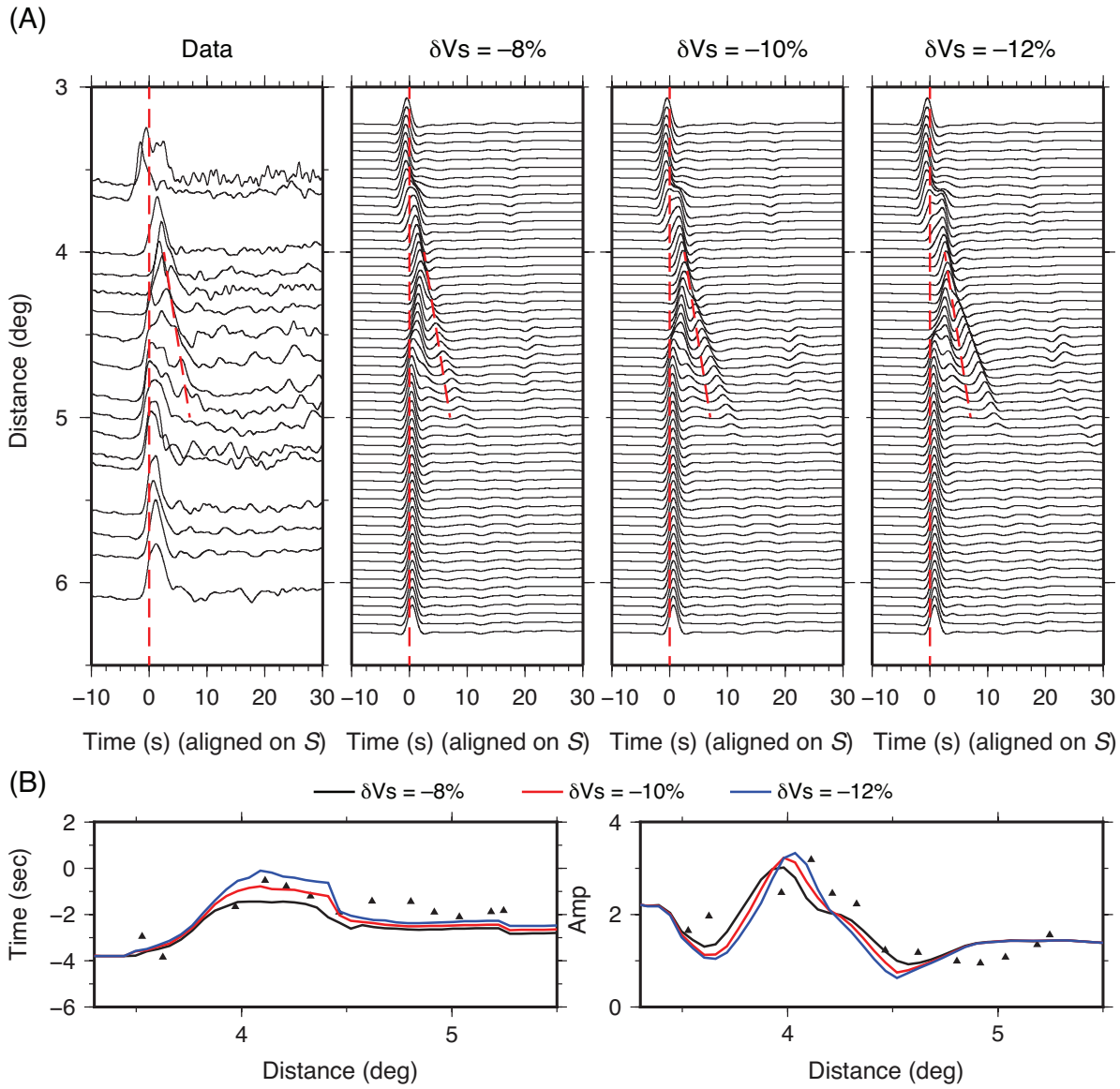
(A)
Data
δVs = –8%
δVs = –10%
δVs = –12%
Distance (deg)
Time (s) (aligned on S)
(B)
δVs = –8%
δVs = –10%
δVs = –12%
Time (sec)
Amp
Distance (deg)

Figure S3

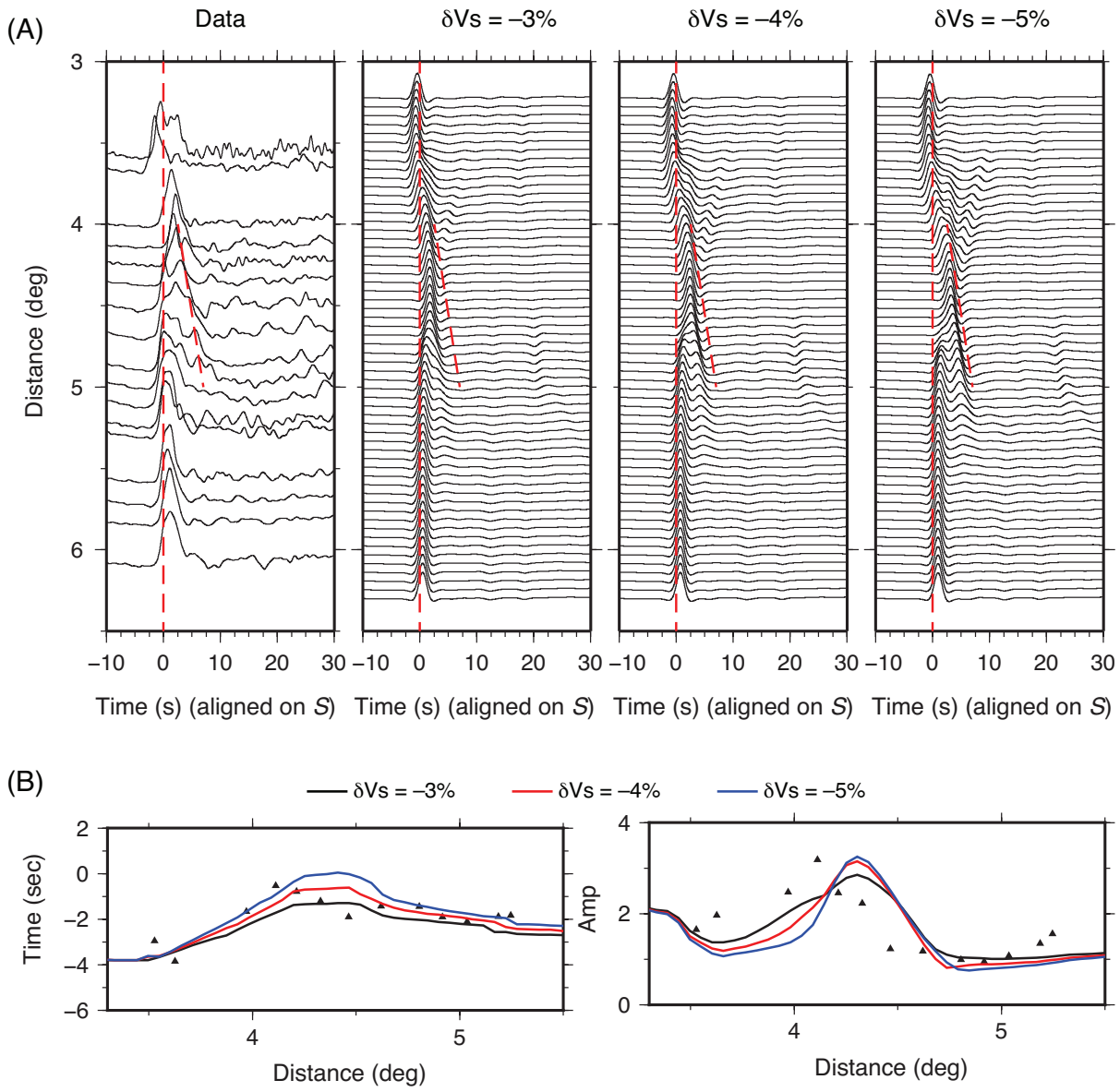
(A)
Data
δVs = –3%
δVs = –4%
δVs = –5%
Distance (deg)
Time (s) (aligned on S)
(B)
δVs = –3%
δVs = –4%
δVs = –5%
Time (sec)
Amp
Distance (deg)

Figure S4

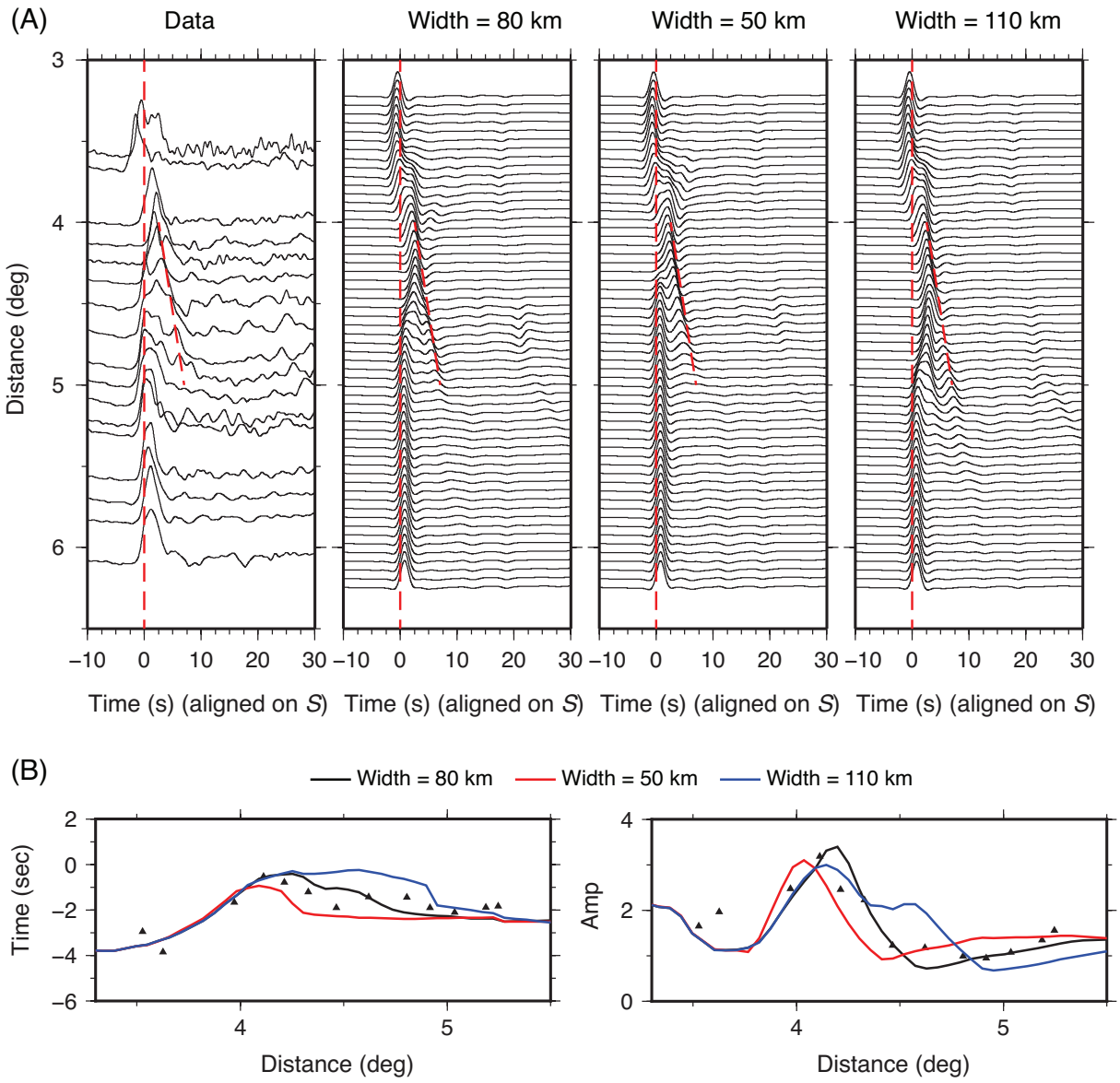
(A)
Data
Width = 80 km
Width = 50 km
Width = 110 km
Distance (deg)
Time (s) (aligned on S)
(B)
Width = 80 km
Width = 50 km
Width = 110 km
Time (sec)
Amp
Distance (deg)

Figure S5

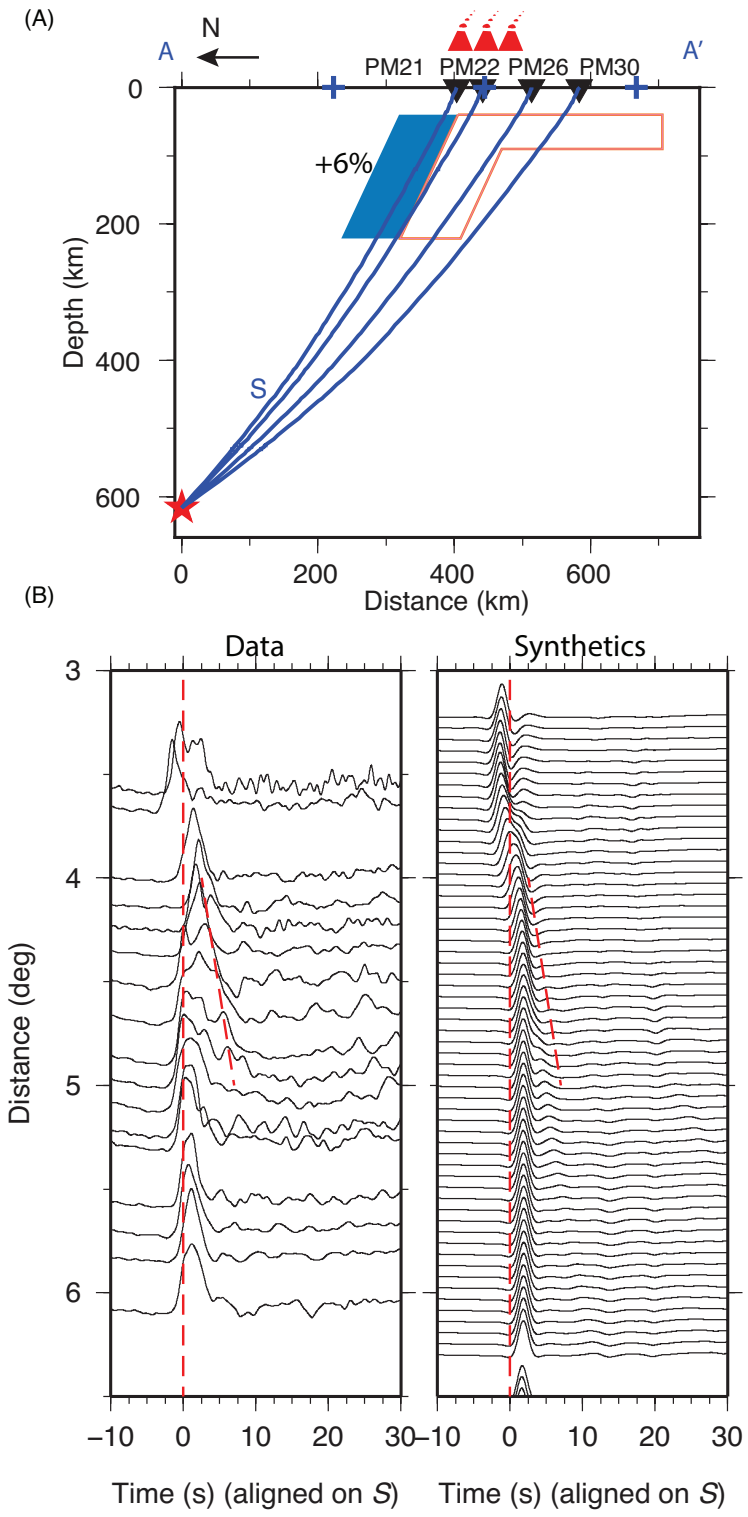
(A)
N
A
A′
PM21
PM22
PM26
PM30
+6%
S
Depth (km)
0
200
400
600
Distance (km)
(B)
Data
Synthetics
Distance (deg)
3
4
5
6
–10
0
10
20
30
Time (s) (aligned on S)
Time (s) (aligned on S)

Figure S6

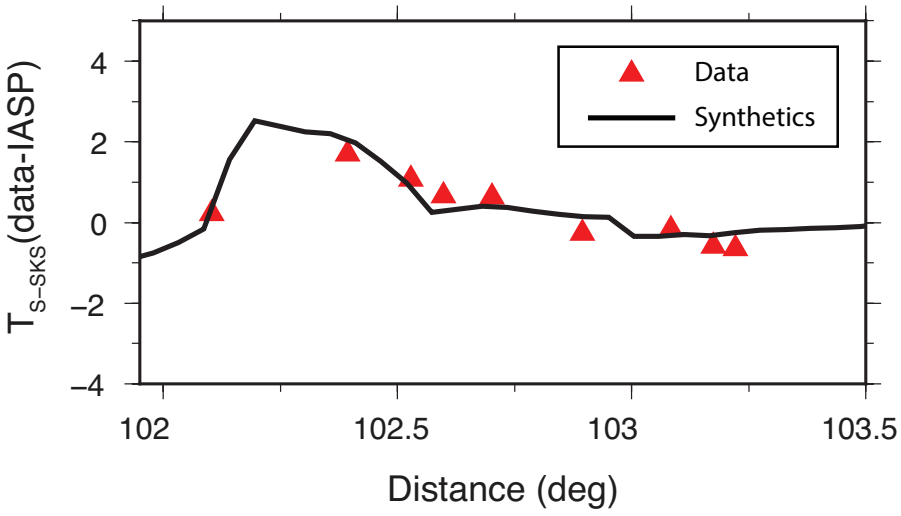
Data
Synthetics
T_{S-SKS}(data-IASP)
4
2
0
−2
−4
102
102.5
103
103.5
Distance (deg)

Figure S7

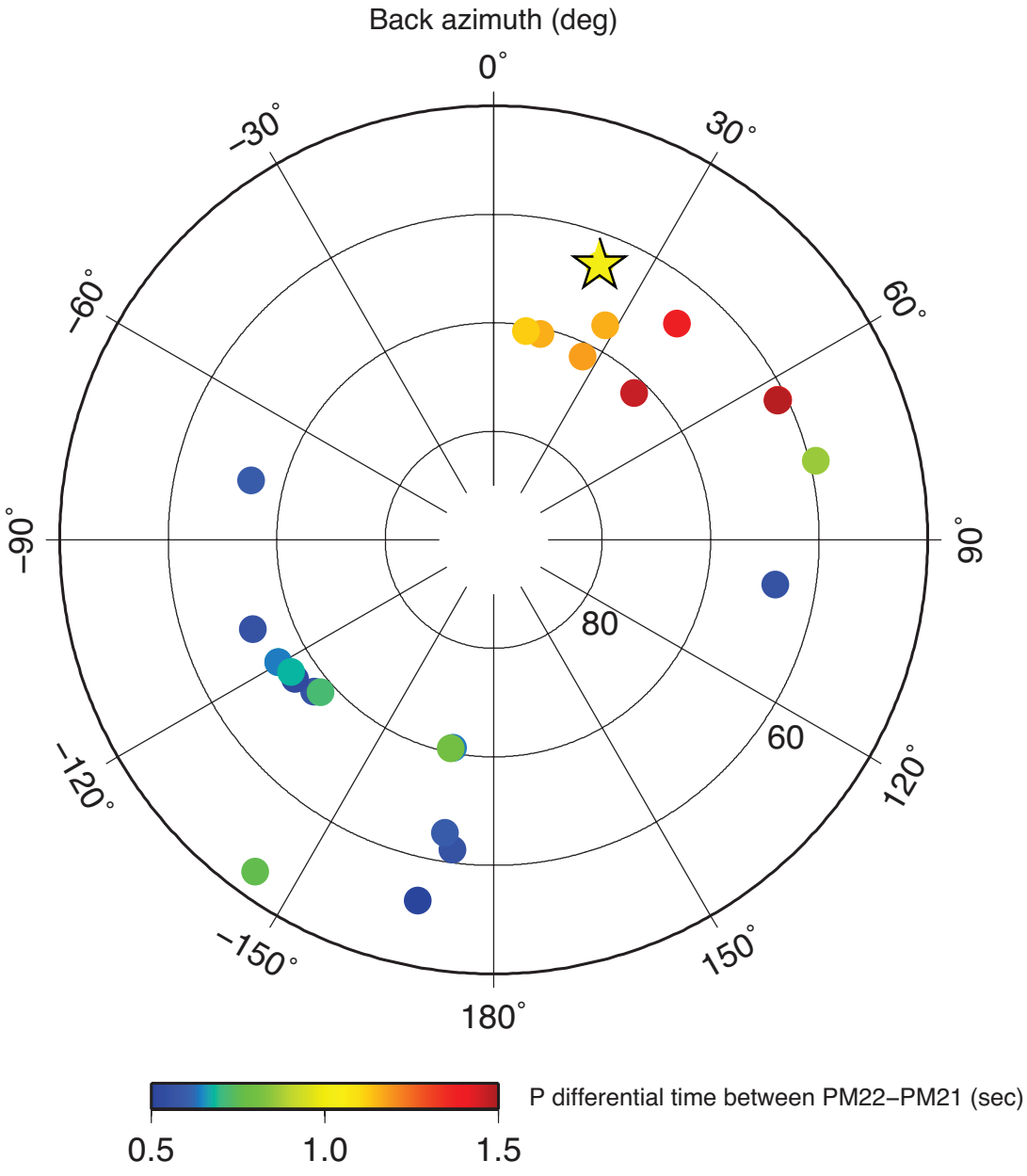
Back azimuth (deg)
0°
30°
60°
90°
120°
150°
180°
−150°
−120°
−90°
−60°
−30°
80
60
P differential time between PM22–PM21 (sec)
0.5
1.0
1.5

Figure S8

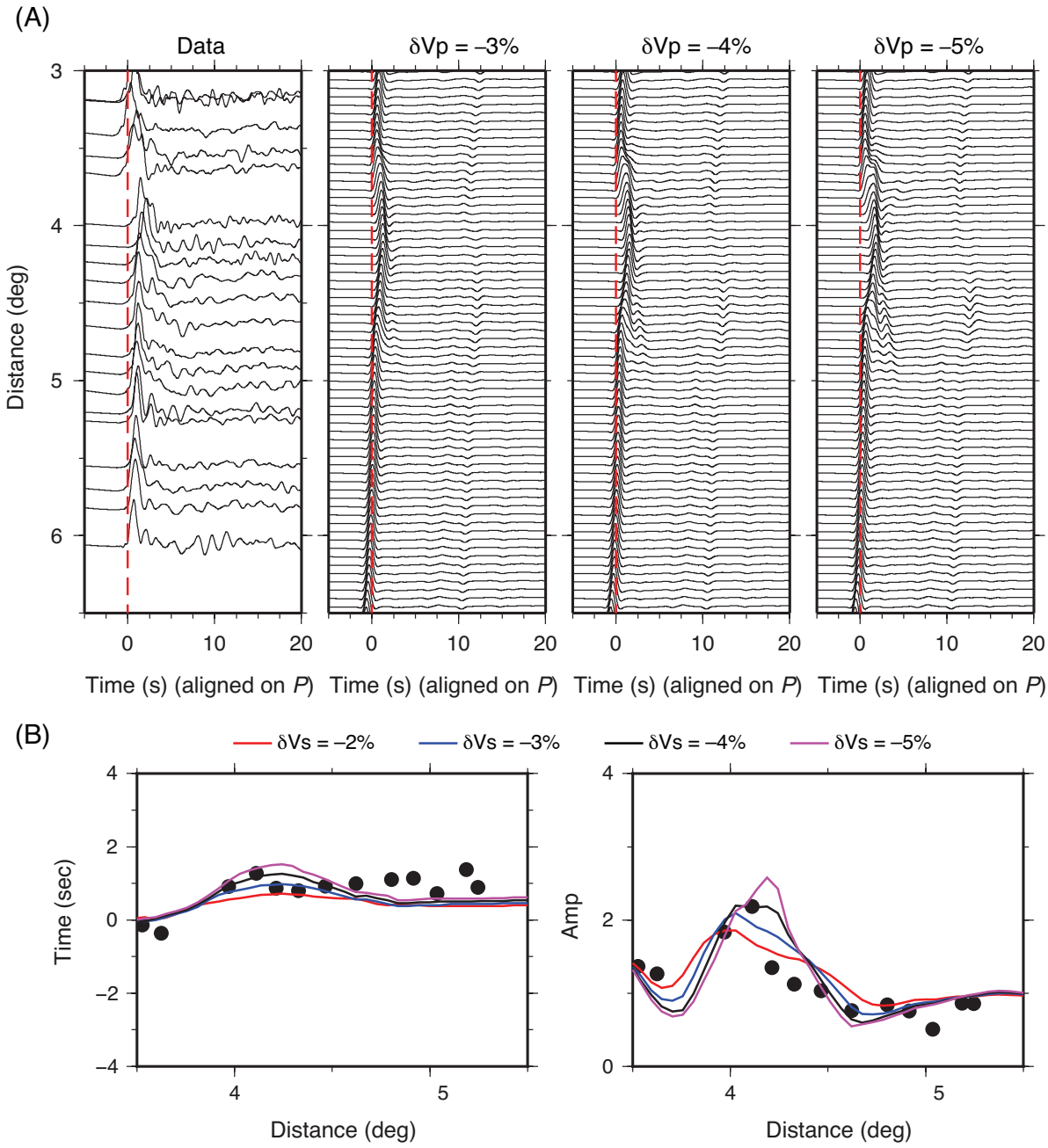
(A)
Data
δVp = –3%
δVp = –4%
δVp = –5%
Distance (deg)
Time (s) (aligned on P)
(B)
δVs = –2%
δVs = –3%
δVs = –4%
δVs = –5%
Time (sec)
Amp
Distance (deg)

Figure S9

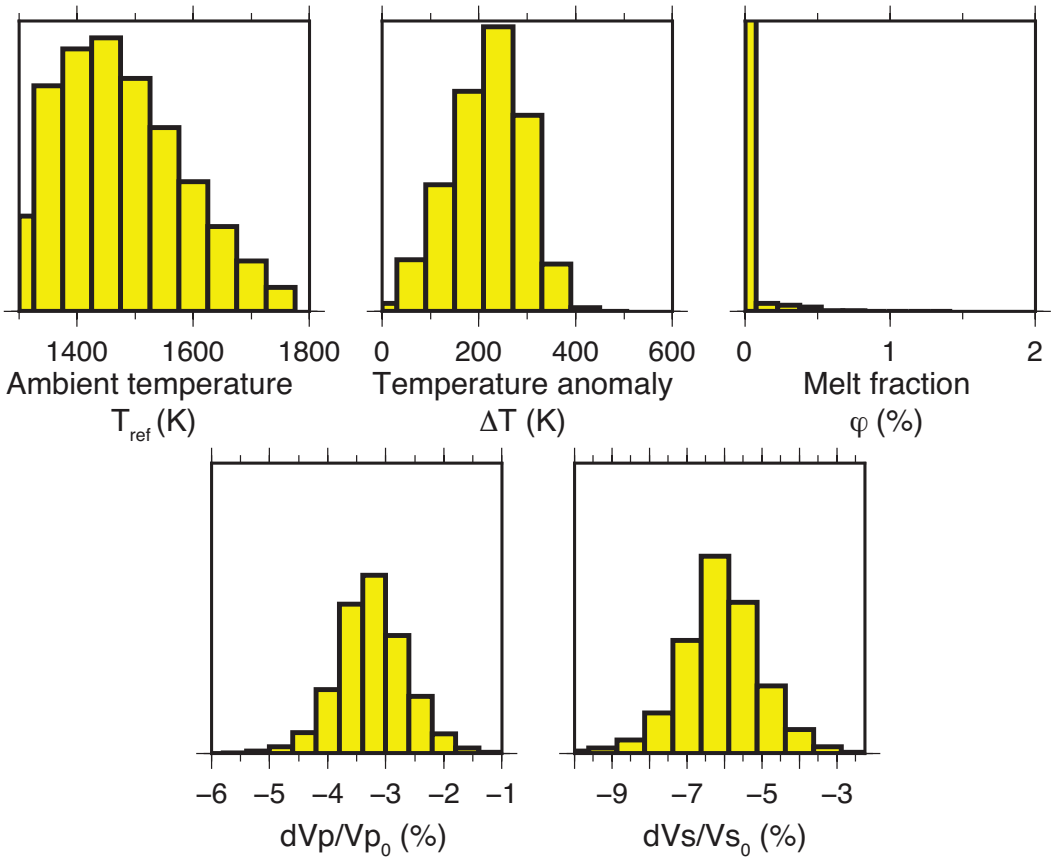
1400
1600
1800
Ambient temperature
T_{ref} (K)
0
200
400
600
Temperature anomaly
ΔT (K)
0
1
2
Melt fraction
φ (%)
−6
−5
−4
−3
−2
−1
dVp/Vp_0 (%)
−9
−7
−5
−3
dVs/Vs_0 (%)

Figure S10